AGU
ADVANCING EARTH AND SPACE SCIENCE

An EISCAT UHF/ESR Experiment That Explains How Ionospheric Irregularities Induce GPS Phase Fluctuations at Auroral and Polar Latitudes

H. M. John[1] , B. Forte[1] , I. Astin[1] , T. Allbrook[2], A. Arnold[3] , B. C. Vani[4] , I. Häggström[5] , and H. Sato[6]

[1]Department of Electronic and Electrical Engineering, University of Bath, Bath, UK, [2]Independent Scholar, Rochester, UK, [3]Independent Scholar, Bristol, UK, [4]Federal Institute of Education, Science and Technology of São Paulo – IFSP, Canindé, Brazil, [5]EISCAT Scientific Association, Kiruna, Sweden, [6]German Aerospace Centre (DLR), Institute for Solar-Terrestrial Physics, Neustrelitz, Germany

Abstract A limitation to the use of Global Navigation Satellite System (GNSS) for precise and real-time services is introduced by irregularities in the ionospheric plasma density. An EISCAT UHF/ESR experiment was conducted to characterize the effect of electron density irregularities on temporal fluctuations in TEC along directions transverse to GPS ray paths in the high latitudes ionosphere. Two representative case studies are described: Enhancements in temporal TEC fluctuations originating (a) in the auroral ionosphere following auroral particle precipitation and (b) in the polar ionosphere following the drift of a polar patch as well as particle precipitation. The results indicate that the origin of enhancements in TEC fluctuations is due to the propagation through large-to-medium scale irregularities (i.e., ranging from few kilometres in the E region to few tens of kilometres in the F region) and occurring over spatial distances of up to approximately 400 km in the E region and up to approximately 800 km in the F region with a patchy distribution. Furthermore, the results indicate that enhancements in TEC fluctuations produced by polar plasma patches and particle precipitation occur over similar temporal scales, thus explaining the overall observation of higher phase scintillation indices in the high-latitude ionosphere. The similarity in the temporal scales over which enhancements in TEC fluctuations occur in the presence of both particle precipitation and plasma patches suggests an intrinsic limitation in the monitoring and tracking of plasma patches through ground GNSS observations.

1. Introduction

The propagation of GNSS signals from satellites to a GNSS receiver on-board an aircraft or on the ground is negatively affected during adverse Space Weather conditions (Lee et al., 2017). Ionospheric disturbances in these conditions cause plasma gradients, which in turn induce fluctuations in the phase and intensity of GNSS signals (Doherty et al., 2004). Phase and intensity fluctuations lead to temporal fluctuations in TEC and scintillation in the received GNSS signals. The presence of gradients through the electron density distribution in the ionosphere can degrade the performance of a GNSS-based infrastructure (Jakowski et al., 2005). Safety-critical applications (Lee et al., 2017), for example, civil aviation, rail transport, autonomous navigation, maritime navigation, oil and gas exploration, precision agriculture, are exposed to significant errors and outages due to enhanced TEC fluctuations and/or scintillation, which can result in the degradation of their performance.

As a radio signal propagates through the ionosphere, electron density irregularities can cause fluctuations in its amplitude and phase (Yeh & Liu, 1982). These fluctuations in the amplitude and phase of the received signal are called amplitude and phase scintillation, respectively (Aarons, 1982). The scintillation activity depends upon the carrier frequency, the time of day, the season of a year, the location, the geomagnetic activity, and the solar cycle (Basu & Basu, 1981). In the equatorial ionosphere, amplitude scintillation can cause deep signal fading challenging the ability of the GNSS receiver to acquire or track the signal. The overall effect of amplitude scintillation is a threat to the availability of service (Walter, 2010). Phase scintillation increases phase noise and causes cycle slips thereby degrading the performance of GNSS and associated technologies (Forte et al., 2017; Jiao et al., 2013; Luo et al., 2018; Walter, 2010; Wernik et al., 2003).
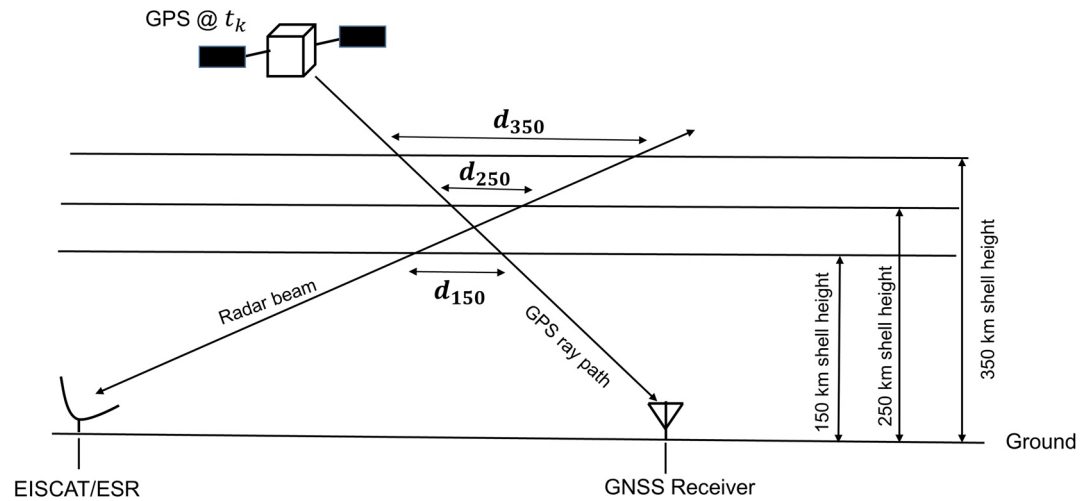
Figure 1. Description of the experiments involving EISCAT UHF/ESR beams transverse to Global Positioning System (GPS) ray paths and separation distances d_{150}, d_{250}, and d_{350} between pierce points at 150, 250, and 350 km ionospheric shell heights, respectively, at specific times t_k. The separation distances d_{150}, d_{250}, and d_{350} are calculated distances between the pierce points of EISCAT UHF/ESR beams and GPS ray paths at 150, 250, and 350 km shell heights, respectively.

This experiment investigated the spatial distribution and size of plasma structures originating temporal phase fluctuations on GPS signals in the auroral and polar ionosphere, by measuring electron density profiles along directions transverse to GPS signals. At high latitudes, GNSS signals tend to experience higher phase fluctuations with lower amplitude fluctuations due to the propagation through larger scale irregularities (Forte & Radicella, 2004; Forte et al., 2017; Keskinen & Ossakow, 1983; Liu et al., 2020): the nature of the temporal phase fluctuations was investigated by considering temporal fluctuations in TEC.

Two representative case studies involving EISCAT (auroral ionosphere), ESR (polar ionosphere) and surrounding GNSS ground stations (from the International GNSS Service, IGS) were considered. Case Study A combined measurement from EISCAT (69.58°N, 19.23°E) and from IGS stations located at Tromsø (TRO1: 69.66°N, 18.94°E), Kilpisjärvi (KILP: 68.94°N, 20.91°E), Hetta (HETT: 68.41°N, 23.67°E), and Kiruna (KIRU: 67.86°N, 20.97°E). Case Study B combined measurements from ESR (78.15°N, 16.02°E) and from IGS stations at Ny-Ålesund (NYAL: 78.9296°N, 11.8651°E), Ny-Ålesund (NYA1: 78.9296°N, 11.8653°E), and Ny-Ålesund (NYA2: 78.9303°N, 11.8586°E). The design of the experiment follows from experiments and results presented in Forte et al., (2013, 2017) where EISCAT measurements were obtained along a given GPS raypath from Tromsø. In this case, EISCAT UHF/ESR beams were along directions transverse to GPS ray paths, thus sampling the ionospheric volume where GPS ray paths propagated.

The experiment addressed the following questions: (a) what is the scale size of irregularities inducing enhancements in TEC fluctuations in both the auroral and polar ionosphere; (b) what is the nature of enhancements in temporal TEC fluctuations in relation to irregularities detected through EISCAT UHF/ESR.

2. Data and Methodology

Electron density profiles were measured along directions transverse to GPS ray paths that propagated toward ground GNSS stations in the surrounding of EISCAT and ESR. In the design of the experiment, the positions of the beams were aimed at different shell heights transverse to possible GPS ray paths in an effort to identify irregularities in both the E and F region. The compromise between mechanical limitations of the radar antenna and the movement of the GPS ray paths led to a separation distance between the pierce points of radar beams and GPS ray paths at those shell heights (Figure 1). Figure 1 illustrates the geometry of the experiment, where d_{150}, d_{250}, and d_{350} are the separation distances between EISCAT UHF/ESR beam and GPS raypath at 150, 250, and 350 km ionospheric shell heights and at time t_k, respectively (only GPS was
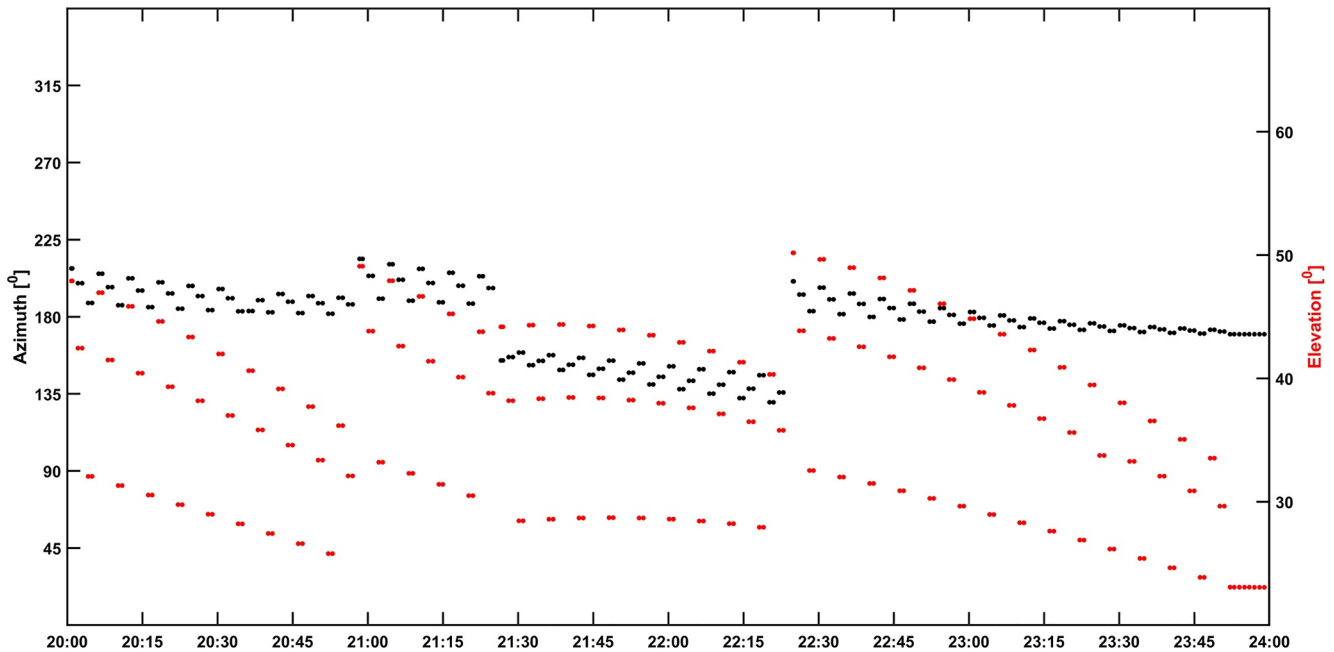
Figure 2. Azimuth (black dots) and elevation (red dots) angles of EISCAT (auroral ionosphere) beams at 60-s integration time designed to sample the volume where many GPS ray paths propagated. The beams were aimed at intersecting shell heights at 150, 250, and 350 km between 20:00 and 24:00 UT in relation to possible Global Positioning System (GPS) ray paths propagating to the ground IGS station in Kiruna. The GPS ray paths considered were those estimated in relation to PRNs 26 (20:00–21:00 UT), 16 (21:00–21:30 UT), 21 (21:30–22:30 UT), and 27 (22:30–24:00 UT) propagating toward Kiruna on March 15, 2018.

considered here). Furthermore, EISCAT UHF/ESR 32 m dish antennas have only two degrees of freedom: thus, few seconds are necessary to re-position the antennas toward a new position of GPS ray paths.

Approximated estimates for azimuth and elevation angles of specific GPS PRNs as observed from Kiruna (in the case of EISCAT) and from Ny-Ålesund (in the case of ESR) were predicted from https://calsky.com as an indication of possible trajectories of GPS satellites in view. The forecasts were used to determine the direction of EISCAT UHF/ESR beams toward different shell heights and given GPS ray paths.

Given that EISCAT UHF/ESR radars can measure only above minimum elevation angles of 23° and 30°, respectively (Spicher et al., 2020), their beams were ideally aimed at intersecting GPS ray paths to Kiruna (Figure 2) and Ny-Ålesund (Figure 3) at 150, 250, and 350 km ionospheric shell heights. That is, the GPS ray paths considered were those approximately estimated in relation to PRNs 26 (20:00–21:00 UT), 16 (21:00–21:30 UT), 21 (21:30–22:30 UT), and 27 (22:30–24:00 UT) propagating toward Kiruna on March 15, 2018, whereas PRNs 26 (20:00–21:00 UT), 16 (21:00–21:30 UT), and 27 (21:30–24:00 UT) propagating toward Ny-Ålesund were considered in the case of ESR on March 16, 2018. However, due to inaccuracies in the orbits predictions and to mechanical constraints with the re-positioning of the radars, there was effectively a separation distance between the radars' beams and the GPS ray paths. Although these aspects introduced limitations in the identification of structures responsible for enhancements in TEC fluctuations, the experiments could still reveal the scale size of the irregularities forming in the high-latitude ionosphere as well as the spatial distance over which they occur and distribute.

EISCAT UHF/ESR measured profiles of electron density, electron temperature, ion temperature, and ion drift velocity (Beynon & Williams, 1978; Forte et al., 2017) with a range resolution that varies between approximately few kilometres in range in the E region to few tens of kilometres in range in the F region (Forte et al., 2017). Results for the measurements collected on March 15 and 16, 2018 are presented and discussed here. EISCAT UHF/ESR raw data were calibrated through GUISDAP (Forte et al., 2013). The errors observed in the electron density profiles tend to decrease with increasing integration time (Forte et al., 2013) and tend to increase with range. Herein, an integration time of 1-min was selected to facilitate the comparison with GPS TEC fluctuations and to guarantee confidence in the measurements.
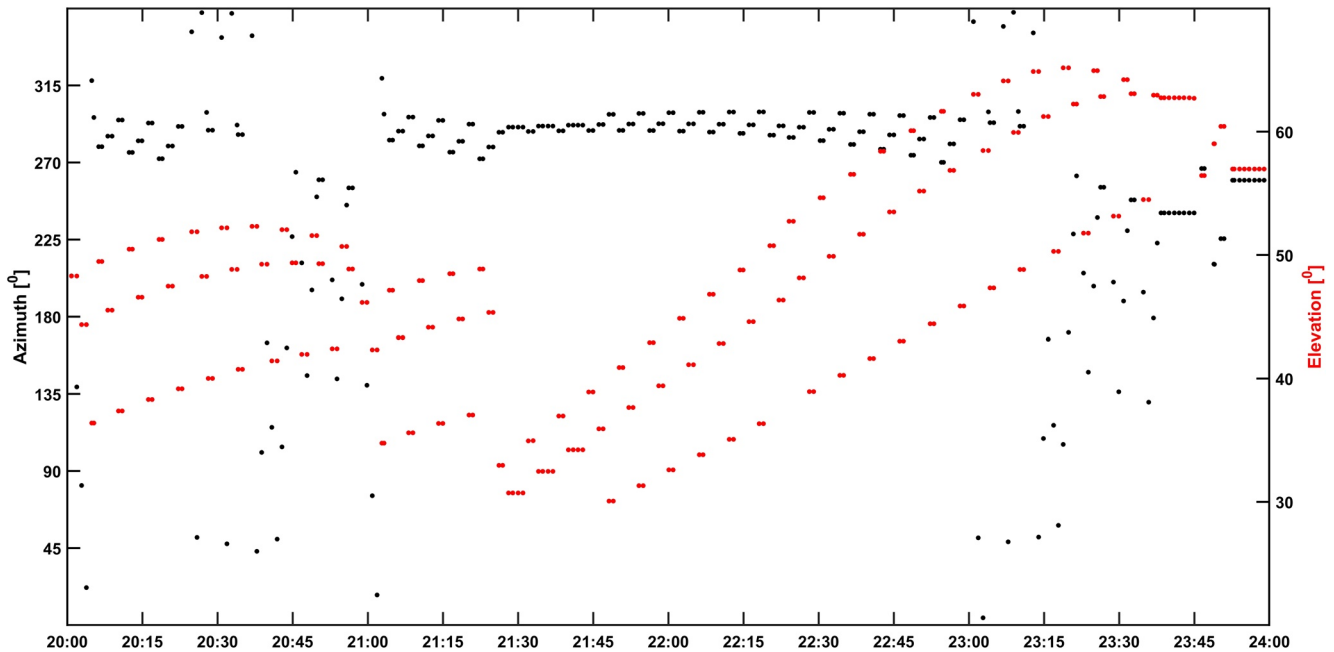
Figure 3. Azimuth (black dots) and elevation (red dots) angles of ESR (polar ionosphere) beams at 60-s integration time designed to sample the volume where many Global Positioning System (GPS) ray paths propagated. The beams were aimed at intersecting shell heights at 150, 250, and 350 km between 20:00 and 24:00 UT in relation to possible GPS ray paths propagating to the ground IGS station in Ny-Ålesund. The GPS ray paths considered were those estimated in relation to PRNs 26 (20:00–21:00 UT), 16 (21:00–21:30 UT), and 27 (21:30–24:00 UT) propagating to Ny-Ålesund on March16, 2018. ESR beams resorted to north-south scans from 20:30 to 21:00 UT and 23:00 to 24:00 UT due to mechanical constraints of the radar antenna.

The rate of change of TEC (ΔTEC/Δt) (Jacobsen & Dähnn, 2014; Luo et al., 2018; and references therein) was calculated from 30-s as well as 1-s Receiver Independent Exchange Format (RINEX) data (ftp://cddis. gsfc.nasa.gov/gnss/data/highrate) collected through geodetic GNSS multi-frequency and multi-constellation receivers. The RINEX data corresponding to several geodetic receivers were downloaded from the Crustal Dynamics Data Information System (CDDIS) (Noll, 2010). The 30-s and as 1-s RINEX observables were read through the gLAB software (https://gage.upc.edu/gLAB/) (Hernandez-Pajares et al., 2010) and the uncalibrated Slant TEC (STEC) was estimated through the combination of carrier phases at L1 and L2 (Ciraolo et al., 2007; Krypiak-Gregorczyk & Wielgosz, 2018).

Temporal TEC fluctuations ΔTEC/Δt were estimated as the difference in STEC between consecutive epochs (Pi et al., 1997):

$$\frac{\Delta \text{TEC}}{\Delta t} = \frac{\text{TEC}(k) - \text{TEC}(k-1)}{\Delta t}\left[\text{TEC}U/\Delta t\right] \tag{1}$$

where $1\,\text{TEC}U = 10^{16}$ electrons/m^2, $\text{TEC}(k)$ is STEC at epoch k, $\text{TEC}(k-1)$ is STEC at epoch $k-1$, and Δt is the time step (Forte et al., 2013; Luo et al., 2018). In Equation 1, Δt can be 30 s or 1 s depending upon the temporal resolution of the RINEX observables.

The structures observed on the electron density profiles were compared with TEC fluctuations observed along various GPS ray paths observed from IGS stations surrounding EISCAT UHF/ESR, as ΔTEC/Δt with $\Delta t = 30$ s is often used to statistically identify and quantify larger scale electron density irregularities (Keskinen & Ossakow, 1983; Pi et al., 1997).

In these experiments which were conducted at auroral and polar latitudes, indices for amplitude scintillation and phase scintillation were not considered because phase fluctuations at L band and over typical GNSS geometries in the high-latitude ionosphere are induced by large-to-medium scale irregularities rather than small-scale irregularities (Forte & Radicella, 2002; Forte et al., 2017). Hence, the investigation considered only temporal TEC fluctuations calculated from 30-s and 1-s GNSS observables to infer phase fluctuations arising from large-to-medium scale irregularities (Keskinen & Ossakow, 1983).
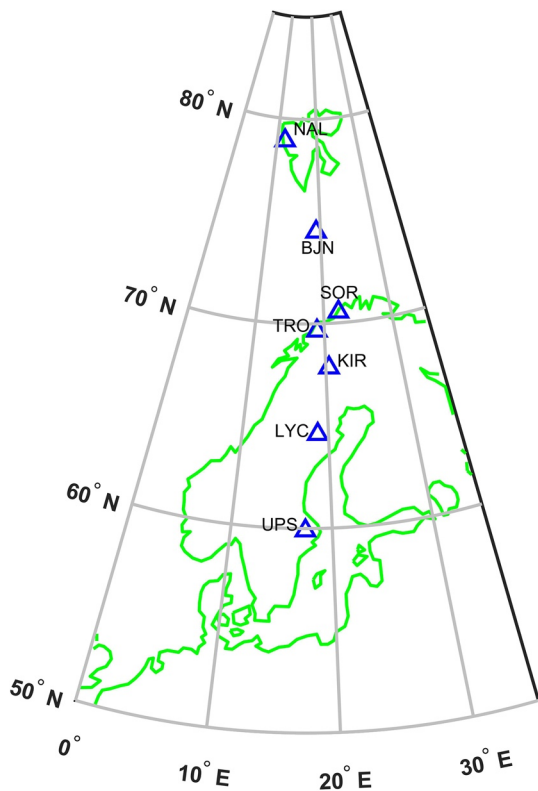
Figure 4. Map of IMAGE stations indicated by ▲ (blue) at NAL (Ny-Ålesund), BJN (Bear Island), SOR (Sørøya), TRO (Tromsø), KIR (Kiruna), LYC (Lycksele), and UPS (Uppsala) between geographic latitudes 59.90°N and 78.92°N (https://space.fmi.fi/image/www/index.php?page=user_defined).

Several magnetometers in a latitudinal chain from the IMAGE network were also considered (Figure 4) to assess the geomagnetic conditions and to infer the presence of particle precipitation in the auroral and polar ionospheres. IMAGE data were obtained from the Finnish Meteorological Institute data repository available at https://space.fmi.fi/image/www/index.php?page=user_defined. The local geomagnetic field components H, D, and Z were calculated from the measured X, Y, and Z components as (Jiao & Morton, 2015; Schunk & Nagy, 2009):

$$H = \sqrt{X^2 + Y^2} \qquad \left[nT\right] \tag{2}$$

$$D = \tan^{-1}\frac{Y}{X} \qquad \left[nT\right] \tag{3}$$

Therefore, variations in H, D, and Z (ΔH, ΔD, and ΔZ, respectively) are given by:

$$\Delta H = H - \langle H \rangle \qquad \left[nT\right] \tag{4}$$

$$\Delta D = D - \langle D \rangle \qquad \left[nT\right] \tag{5}$$

$$\Delta Z = Z - \langle Z \rangle \qquad \left[nT\right] \tag{6}$$

where $\langle H \rangle$, $\langle D \rangle$, and $\langle Z \rangle$ are the temporal averages of H, D, and Z, calculated as $\langle H \rangle = 1/N \sum_{i=1}^{N} H_i$, $\langle D \rangle = 1/N \sum_{i=1}^{N} D_i$, and $\langle Z \rangle = 1/N \sum_{i=1}^{N} Z_i$, respectively, where N is the number of observations. Here, $N = 1440$ corresponding to 1-min sampling and $\langle H \rangle$, $\langle D \rangle$, and $\langle Z \rangle$ are the averages computed over the 24 h. The computed averages are then subtracted from the actual observations (H, D, and Z) to get the corresponding magnetic variations (ΔH, ΔD, and ΔZ). A negative H component variation suggests the presence of substorm which is often associated with particle precipitation. For the benefit of this investigation, a 1-min sampling interval was considered in order to align magnetograms with EISCAT UHF/ESR integration time of 1-min (Luo et al., 2018 and references therein).

3. Results

Two case studies referred to as Case Study A and B were considered. Case Study A refers to the results from EISCAT while Case Study B refers to the results from ESR. In general, EISCAT UHF/ESR radar beams can cover a range of about 2000 *km* on average (Tjulin, 2017), with errors in the electron density profiles increasing with range.

3.1. Case Study A: EISCAT, March 15, 2018, 20:00–24:00 UT

Figure 5 shows the measurements collected on March 15, 2018 between 20:00 and 24:00 UT. In Figure 5, from top to bottom, shows profiles of electron density; GPS TEC fluctuations for PRNs 08 (magenta), 16 (blue), 20 (cyan), 21 (green), 10 (yellow), 27 (red), and 26 (black) observed from different geodetic stations, that is, Tromsø (TRO1, dashed lines), Kilpisjärvi (KILP, dotted lines), Hetta (HETT, dash-dotted lines), and Kiruna (KIRU, solid lines); and separation distances d_{150}, d_{250}, and d_{350} between pierce points of GPS ray paths and EISCAT beams at 150, 250, and 350 km shell heights, respectively (Figure 5, bottom three panels). The beams geometry for this case is shown in Figure 2 by means of azimuth and elevation angles of the EISCAT beams. The wave-like patterns visible in the separation distances d_{150}, d_{250}, and d_{350} between ionospheric pierce points of EISCAT beams and of GPS ray paths at 150, 250, and 350 km shell heights are caused by the re-pointing of EISCAT beams from one ionospheric shell height to another during the time of measurements. It is important to note that from all the GNSS receiver stations considered in the experiment, no GPS PRN raypath is intersected by EISCAT beams because the EISCAT beams sit in the middle of the various PRNs ray paths during time of measurements. This way, the radar beams were sampling the ionospheric volume traversed by various GPS ray paths.
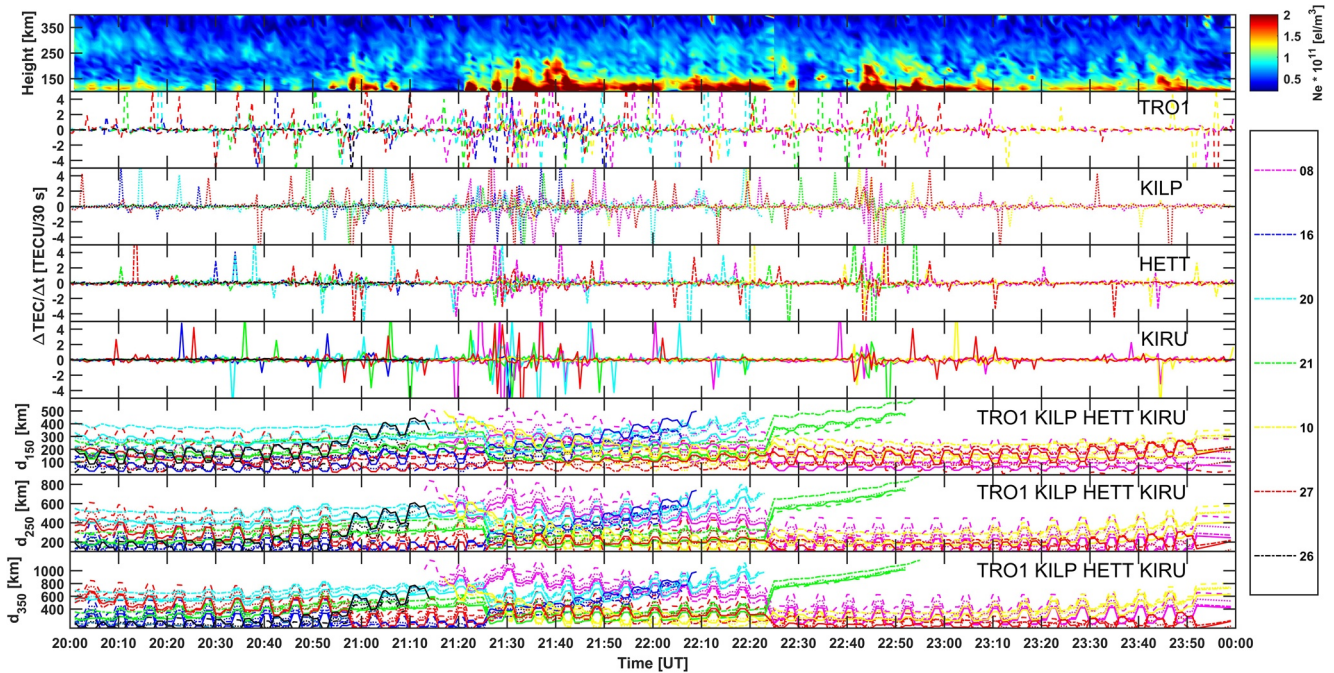
Figure 5. From top to bottom: EISCAT profiles of electron density as function of height; 30-s Global Positioning System (GPS) TEC fluctuations from Tromsø (TRO1, dashed lines), Kilpisjärvi (KILP, dotted lines), Hetta (HETT, dash-dotted lines), and Kiruna (KIRU, solid lines) for GPS PRNs 08 (magenta), 16 (blue), 20 (cyan), 21 (green), 10 (yellow), 27 (red), and 26 (black); separation distances d_{150}, d_{250}, and d_{350} between ionospheric pierce points of EISCAT beams and GPS ray paths at 150, 250, and 350km shell height, respectively between 20:00 and 24:00 UT on March 15, 2018. These separation distances were estimated for all the GNSS ground stations considered (i.e., TRO1, KILP, HETT, and KIRU).

From Figure 5, it is evident that the enhancements in temporal TEC fluctuations observed on various PRNs from different ground stations corresponded to ionisation structures detected by EISCAT. This allowed an estimate of the spatial distance over which irregularities distribute in the ionospheric volume that was sampled.

Figure 6 shows the fluctuations in the *HDZ* geomagnetic field components over Ny-Ålesund (NAL), Bear Island (BJN), Sørøya (SOR), Tromsø (TRO), Kiruna (KIR), Lycksele (LYC), and Uppsala (UPS) stations between 20:00 and 24:00 UT on March 15, 2018. A K_p index of 4 during the time of measurement [ftp://ftp.swpc.noaa.gov/pub/indices/old_indices/] suggests active geomagnetic conditions while the southward *H* component fluctuations (red line) after 22:00 UT (5th panel from top of Figure 6) suggest auroral substorm onset, generally favoring auroral particle precipitation in the E region (Forte et al., 2017). The presence of intermittent and inhomogeneous particle precipitation is further confirmed by optical emissions recorded through the all-sky camera at Kiruna (https://www2.irf.se/allsky/2018/20180315/jpgs/).

Enhancements in the electron density (up to about 1.9×10^{11} electrons/m³) occurred mainly below an altitude of 150 km suggesting the presence of E region structures likely due to auroral particle precipitation. Enhancements in TEC fluctuations within $\pm 5\,TECU/30\,s$ were observed in general between 20:00 and 24:00 UT on GPS signals from geodetic GNSS stations surrounding EISCAT beams. Enhancements in TEC fluctuations intensified when enhancements in electron density extended between 100 and 250 km of altitude. While enhancements in TEC fluctuations due to ionization structures at an altitude of approximately $100 - 150$ km were not observed at every ground station, TEC fluctuations corresponding to electron density structures extending between 100 and 250 km in altitude enhanced simultaneously at all stations (for example, during intervals 21:20–21:50 UT and 22:40–22:50 UT). Overall, those electron density structures detected between 100 and 250 km of altitude and capable of inducing enhancements in TEC fluctuations were likely to occur over spatial distances of up to approximately 400 km in the E region and up to approximately 800 km in the F region as indicated in Figure 5.
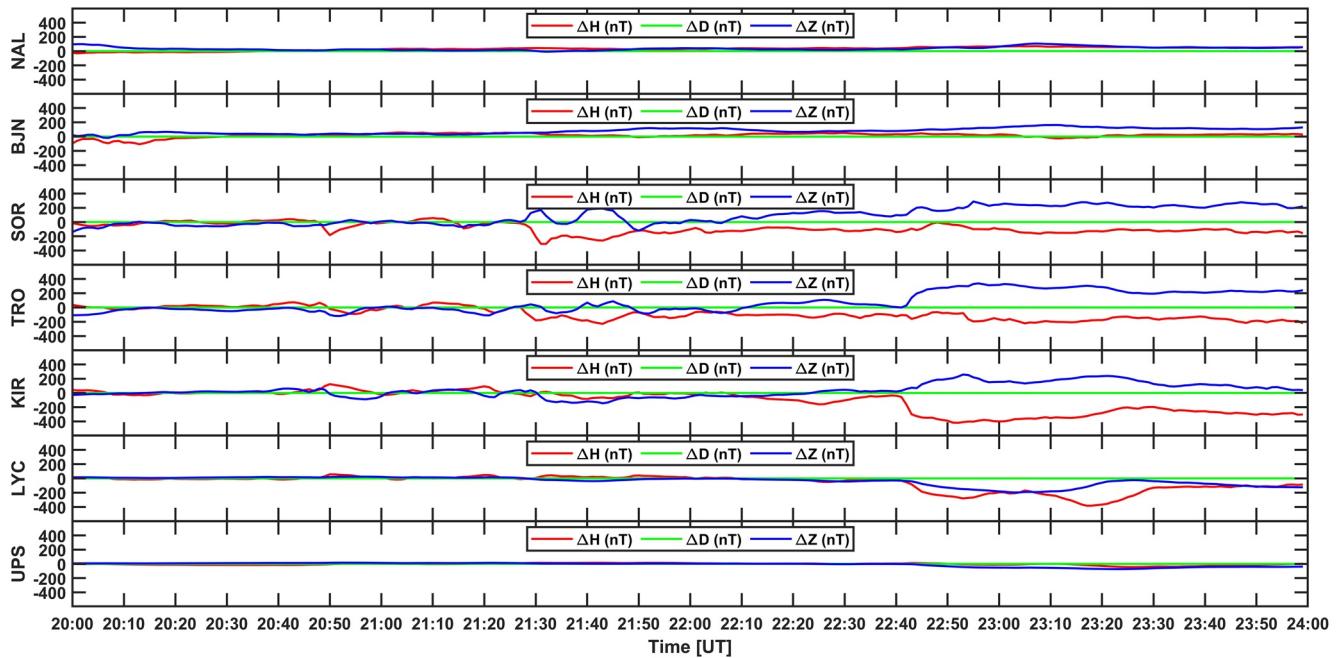
Figure 6. *HDZ* local geomagnetic field components variations (Δ*H*, Δ*D*, and Δ*Z*, in nT) from a latitudinal chain of stations at Ny-Ålesund (NAL), Bear Island (BJN), Sørøya (SOR), Tromsø (TRO), Kiruna (KIR), Lycksele (LYC), and Uppsala (UPS) magnetometer stations, respectively between 20:00 and 24:00 UT on March 15, 2018.

3.2. Case Study B: ESR, March 16, 2018, 20:00–24:00 UT

Figure 7 has the same content as Figure 5 and shows measurements collected through ESR on March 16, 2018 between 20:00 and 24:00 UT. GPS TEC fluctuations for PRNs 08 (magenta), 16 (blue), 20 (cyan), 21 (green), 10 (yellow), 27 (red), and 26 (black) observed from different geodetic stations: Ny-Ålesund (NYAL, dashed lines), Ny-Ålesund (NYA1, dash-dotted lines), and Ny-Ålesund (NYA2, solid lines). In this case, the only available ground IGS stations were indeed those in Ny-Ålesund. The beams geometry for this case is shown in Figure 3 by means of azimuth and elevation angles of the ESR beams. ESR beams had to resort to north-south scans between 20:30–21:00 UT and 23:00–24:00 UT due to mechanical constraints of the radar antenna as shown in Figure 3.

Electron density enhancements (up to about 1.9×10^{11} electrons/m^3) occurred below an altitude of approximately 150 km (21:20–21:30 UT), between approximately 100 and 250 km of altitude (21:40–22:10 UT) and between approximately 100 and 350 km of altitude (21:20–21:40 UT). While the irregularities occurring between 100 and 250 km of altitude appear consistent with particle precipitation due to changes in the geomagnetic field (Figure 9), those occurring between 100 and 350 km of altitude (21:20–21:40 UT) appear to be consistent with the presence of a polar patch traversing the ESR beams and the GPS ray paths. An example of the convection pattern provided by SuperDARN (Figure 8) shows the presence of a fast-moving plasma between 21:20 and 21:40 UT to the north of ESR, suggesting the presence of a polar patch intersected by the ESR beams pointing northward (compare Figure 3 and Figure 8) and causing enhancement in temporal TEC fluctuations (within $\pm 5\,TECU \, / \, 1\,s$). In this case, electron density structures detected between 100 and 350 km of altitude and capable of inducing enhancements in TEC fluctuations were likely to occur over spatial distances of up to approximately 400 km in the E region and up to approximately 800 km in the F region (Figure 7).

In Figure 8, the ESR position is indicated by "LYR" (Longyearbyen) on the convection map: at the time of the measurements Longyearbyen was approximately between 00:30 and 01:00 Magnetic Local Time. Longyearbyen and Ny-Ålesund are in the field of view of some of the SuperDARN radars at a ground distance in excess of 1,000 km on average (http://vt.superdarn.org/tiki-index.php?page=radarFinder). At these distances, the backscatter power originates from irregularities in the F region that move under the effect of the
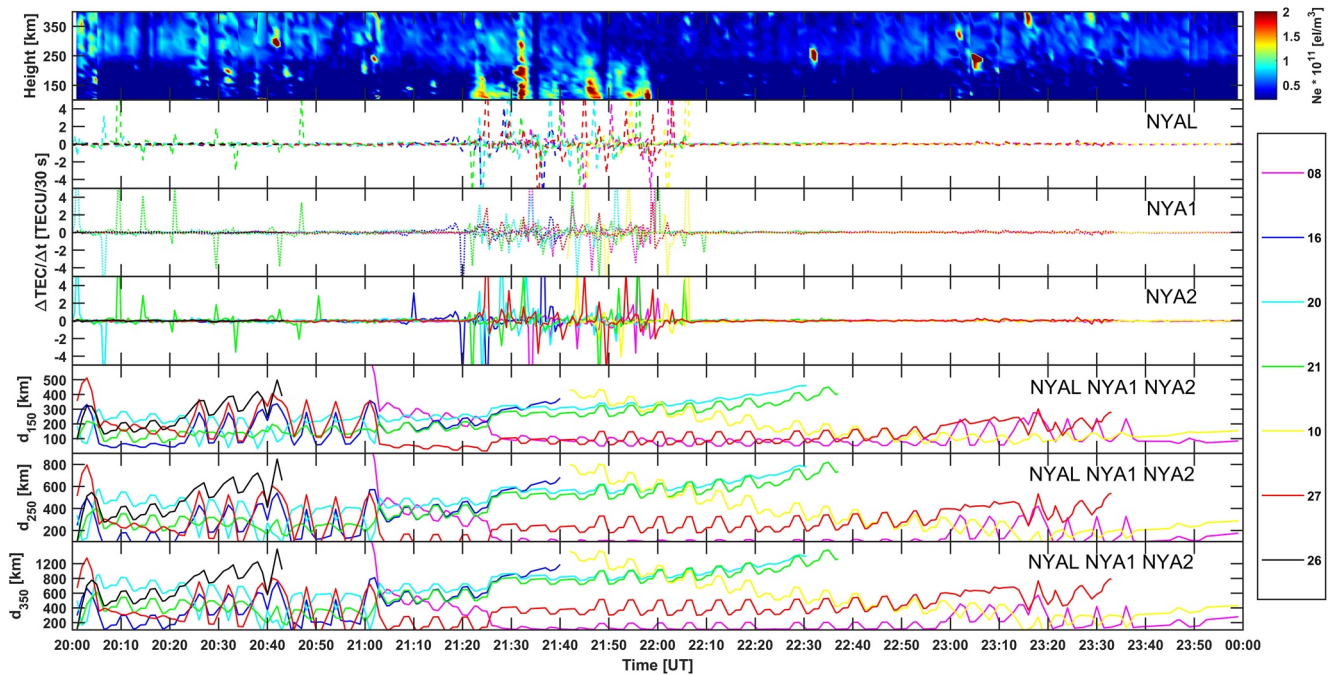
Figure 7. From top to bottom: ESR (polar ionosphere) profiles of electron density as function of height; 30-s GPS TEC fluctuations from Ny-Ålesund (NYAL, dashed lines), Ny-Ålesund (NYA1, dash-dotted lines), and Ny-Ålesund (NYA2, solid lines) for GPS PRNs 08 (magenta), 16 (blue), 20 (cyan), 21 (green), 10 (yellow), 27 (red), and 26 (black); separation distances d_{150}, d_{250}, and d_{350} between ionospheric pierce points of ESR beams and GPS ray paths at 150, 250, and 350 km shell heights, respectively between 20:00 and 24:00 UT on March 16, 2018. These separation distances were estimated for all the GNSS ground stations considered (i.e., NYAL, NYA1, and NYA2).

$E \times B$ plasma drift (Chisham & Pinnock, 2002; Chisham et al., 2008; Prikryl et al., 2010; Thomas & Shepherd, 2018). Therefore, the plasma flow illustrated in Figure 8 in correspondence to the volume sampled by ESR beams refers to irregularities in the F region.

While the irregularities occurring within 100 to 250 km of altitude between 21:20–21:30 UT and 21:40–22:10 UT appear consistent with particle precipitation due to changes in the geomagnetic field (Figure 9), those occurring between 100 and 350 km of altitude (21:20–21:40 UT) appear to be consistent with the presence of a polar patch traversing the ESR beams and the GPS ray paths.

4. Discussions

The origin of GPS phase fluctuations in the auroral and polar ionospheres was investigated through an EISCAT UHF/ESR experiment aimed at characterizing the electron density distribution along profiles transverse to GPS ray paths. In general, EISCAT UHF/ESR beams were alternately re-positioned to sample the volume where various GPS ray paths propagated in the auroral/polar ionosphere. Based on the results, it seems plausible to conclude that enhancements in TEC fluctuations observed in Case Study A (EISCAT on March 15, 2018, auroral ionosphere) were caused by electron density irregularities arising from auroral particle precipitation. On the other hand, enhancements in TEC fluctuations observed in Case Study B (ESR on March 16, 2018, polar ionosphere) were caused by electron density irregularities arising from both a polar cap patch and particle precipitation (Prikryl et al., 2010).

While the polar cap patch in Case Study B was drifting at a velocity of the order of 550 m/s (Figure 8), no significant plasma drift was observed in the case of particle precipitation for both Case Studies A and B (convection maps for these cases are available at http://vt.superdarn.org/tiki-index.php?page=Conv+map+overview). Yet, enhanced temporal TEC fluctuations were observed on GPS signals in both cases. In both case studies, the distance between the pierce points of GPS ray paths (showing enhanced TEC fluctuations simultaneously at various stations) and the pierce points of EISCAT UHF/ESR beams at several
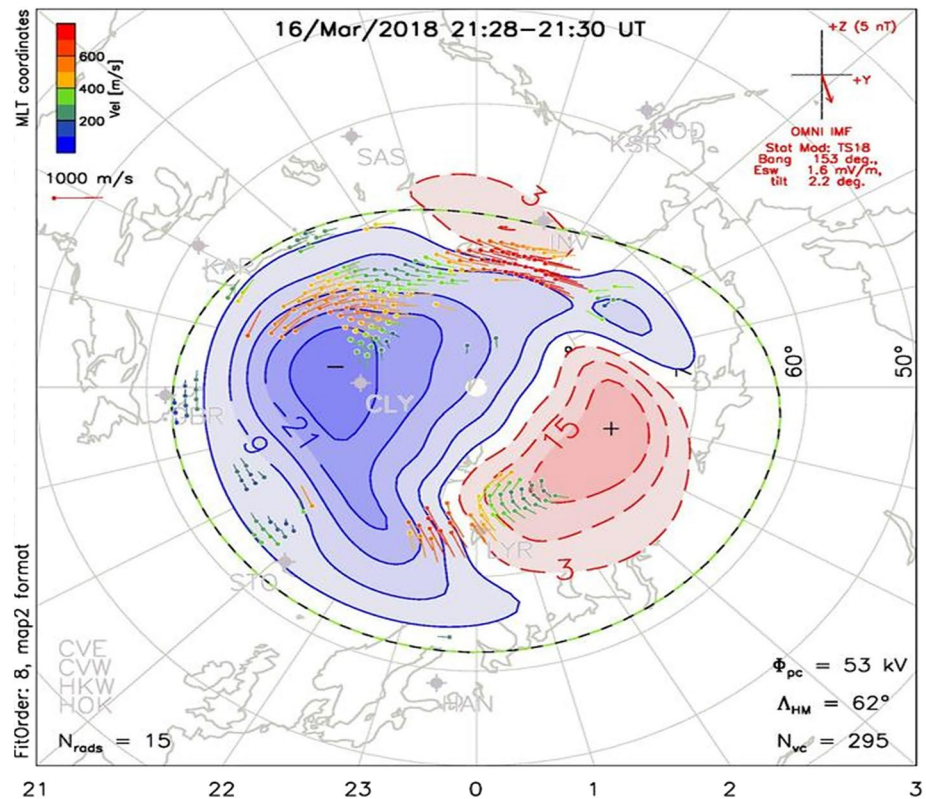
Figure 8. Convection maps pattern estimated through SuperDARN from 21:28 to 21:30 UT on March 16, 2018. Ny-Ålesund is located approximately 127km North-West of Longyearbyen (herein labeled as "LYR" on the convection map). The green dashed curve represents the Heppner-Maynard Boundary (Courtesy of College of Engineering, VirginiaTech SuperDARN). Additional convection maps are available at http://vt.superdarn.org/tiki-index.php?page=Conv+map+overview.

shell heights indicate that electron density irregularities occurred and were distributed over spatial distances of up to approximately 400 km in the E region and up to approximately 800 km in the F region.

There are two important questions about the observations presented here: (a) what is the scale size of the irregularities as detected in both the auroral and polar ionosphere by means of the radars and the GPS links and (b) what is the nature of the enhancements in GPS TEC fluctuations: that is, whether the signature on GPS TEC fluctuations is different between particle precipitation and polar patches (this would imply a clear way to distinguish between particle precipitation and plasma patches by utilizing ground GNSS observations that can be used, for example, to track the temporal and spatial evolution of polar plasma patches).

Although an important limitation of these observations is that neither EISCAT UHF/ESR nor GPS can resolve the spatial and temporal variability of the irregularities at the same time, two considerations about the nature of the irregularities detected can still be made to some extent.

Given that TEC fluctuations were enhanced in the presence of both particle precipitation and a polar plasma patch, the first consideration is about the temporal scale of the TEC fluctuations detected on GPS signals in the auroral (Case Study A) and polar (Case Study B) ionospheres. GPS TEC fluctuations were detected on several links from various ground stations in the surrounding of both EISCAT and ESR, suggesting that irregularities were distributed over a wide area in conjunction with particle precipitation for Case Study A and to a plasma patch for Case Study B.

In order to investigate further on the temporal scale of the GPS TEC fluctuations, 1-s observables were utilized to estimate 1-s TEC fluctuations: a few representative PRNs were selected from the ground stations in Kiruna (PRN08, PRN10, PRN21, and PRN27) and in Ny-Ålesund (PRN08, PRN20, PRN21, and PRN27).
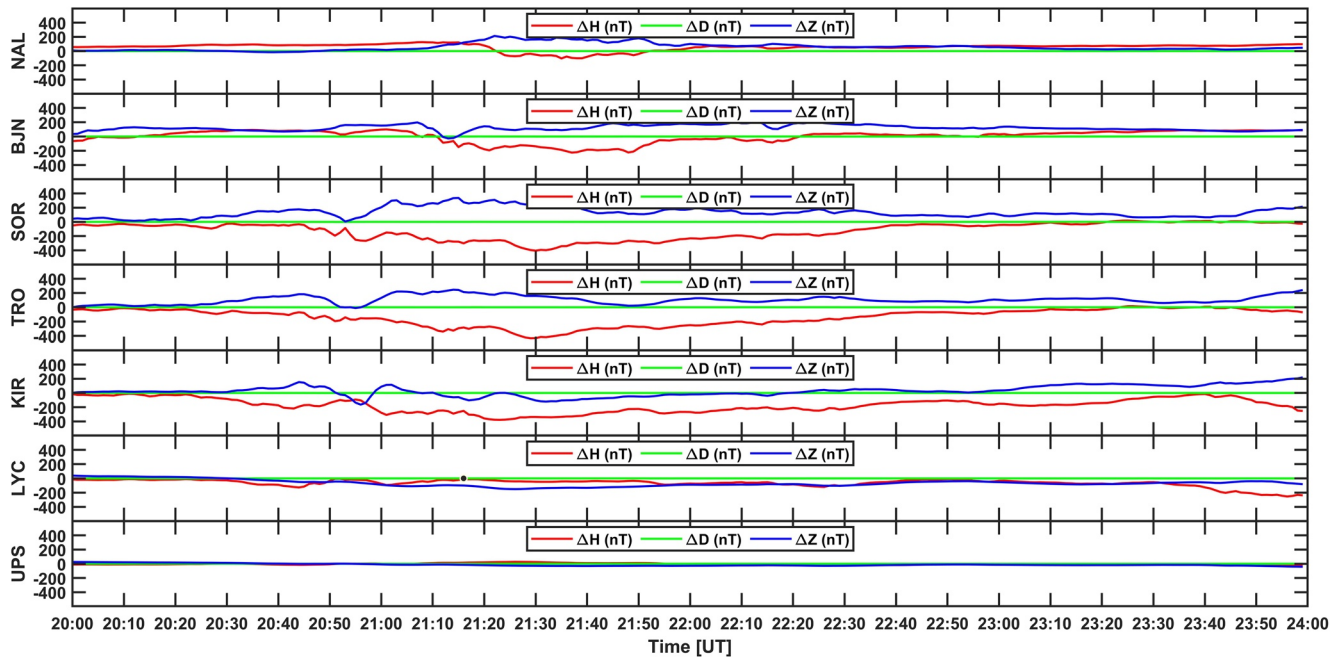
Figure 9. *HDZ* local geomagnetic field components variations(∆*H*, ∆*D*, and ∆*Z*, in nT) from a latitudinal chain of stations at Ny-Ålesund (NAL), Bear Island (BJN), Sørøya (SOR), Tromsø (TRO), Kiruna (KIR), Lycksele (LYC), and Uppsala (UPS) magnetometer stations, respectively between 20:00 and 24:00 UT on March 16, 2018.

The 1-s TEC fluctuations observed between 20:00 and 24:00 UT on the signals observed from Kiruna are illustrated in Figure 10a and those observed from Ny-Ålesund are illustrated in Figure 10b.

The 1-s observables were considered instead of 30-s observables, in order to estimate the autocorrelation function of TEC fluctuations, as follows. The autocorrelation function for the 1-s TEC fluctuations time series shown in Figure 10a was estimated over 2-min temporal intervals between 20:00 and 24:00 UT, after discarding spikes introduced by cycle slips. The correlation time in each of the 2-min intervals was estimated by linearly interpolating the autocorrelation function at 1 ms intervals (given a 1 s sampling interval for the original TEC observations) and by deducing the time interval at which the autocorrelation function dropped to a value of 1/2 (similar estimates can be obtained by utilizing a value of 1/e though the order of magnitudes for these estimates within the available temporal resolution would be very similar). The correlation time in the case of the selected PRNs (Figure 10a) observed from Kiruna is illustrated in Figure 10c, whereas the correlation time in the case of the selected PRNs (Figure 10b) observed from Ny-Ålesund is illustrated in Figure 10d.

Although an increase in the correlation time can occur in the absence of enhancements in TEC fluctuations (e.g., PRN21), in the presence of enhanced TEC fluctuations the correlation time generally tends to increase in both case studies A and B (e.g., PRN27). This indicates that as the GPS ray paths scan through irregularities formed in conjunction with particle precipitation in the auroral ionosphere as well as with a plasma patch in the polar ionosphere the variation in the rate of change of TEC generally occurs over longer temporal scales (Figures 10c and 10d): Longer temporal scales imply a larger scale size for the irregularities traversed by the ray paths.

The fact that the enhancements in TEC fluctuations occur over longer temporal scales is supported by details on how the autocorrelation function varies in the case of observations from both Kiruna and Ny-Ålesund, which few examples of are illustrated in Figure 11. Figure 11a illustrates TEC fluctuations for PRN08 observed from Kiruna, Case Study A March 15, 2018, in specific 2-min intervals corresponding to increased ionisation due to auroral particle precipitation detected through EISCAT (Figure 5); Figure 11b illustrates TEC fluctuations for PRN08 observed from Ny-Ålesund, Case Study B March 16, 2018, in specific 2-min intervals corresponding to the drift of a polar plasma patch and particle precipitation detected
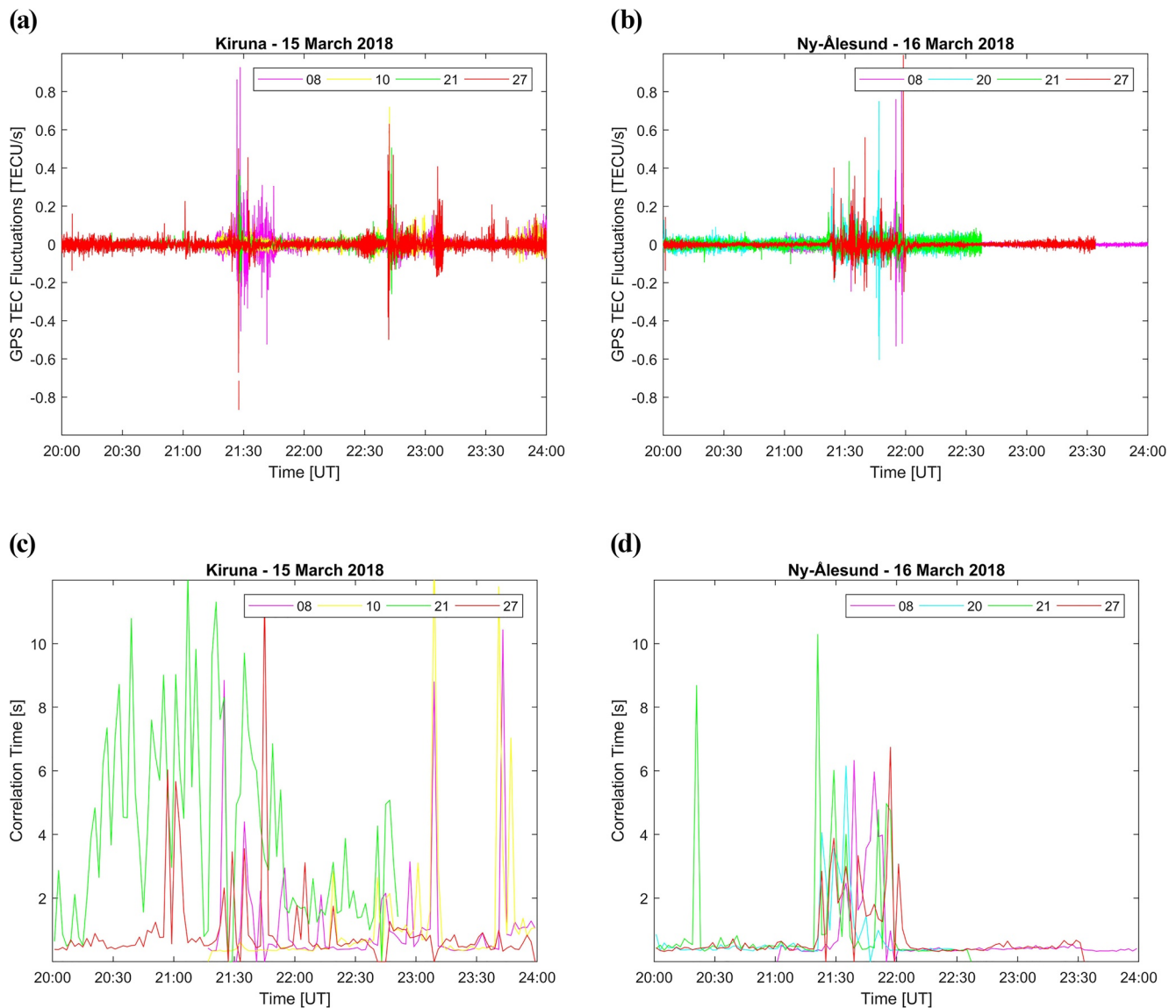
Figure 10. 1-s Global Positioning System (GPS) TEC fluctuations for Case Study A on PRNs observed from Kiruna and for Case Study B on PRNs observed from Ny-Ålesund. (a) TEC fluctuations for PRN08 (magenta), PRN10 (yellow), PRN21 (green), and PRN27 (red) from Kiruna, Case Study A, March 15, 2018. (b) 1-s TEC fluctuations for PRN08 (magenta), PRN20 (cyan), PRN21 (green), and PRN27 (red) from Ny-Ålesund, Case Study B, March 16, 2018. (c) Correlation interval for PRN08 (magenta), PRN10 (yellow), PRN21 (green), and PRN27 (red) between 20:00 and 24:00 UT corresponding to TEC fluctuations measured from Kiruna, Case Study A. (d) Correlation interval for PRN08 (magenta), PRN20 (cyan), PRN21 (green), and PRN27 (red) between 20:00 and 24:00 UT corresponding to TEC fluctuations measured from Ny-Ålesund, Case Study B.

through ESR (Figure 7). The autocorrelation function calculated for each of these 2-min intervals is illustrated in Figure 11c (in relation to TEC fluctuations shown in Figure 11a) and in Figure 11d (in relation to TEC fluctuations shown in Figure 11b).

During enhancements in TEC fluctuations the autocorrelation function widens indicating the presence of a trend in the GPS TEC fluctuations and leading to an increase in the correlation time (Figure 10). This fact is consistent with the presence of larger-scale irregularities traversed by the GPS ray paths during particle precipitation in the auroral ionosphere (Kiruna, Case Study A) and during the transit of a plasma patch in the polar ionosphere (Ny-Ålesund, Case Study B).

Given that the radar beams were sparsely sampling the volume traversed by various GPS ray paths experiencing enhancements in TEC fluctuations, the second consideration is about the spatial scale of the
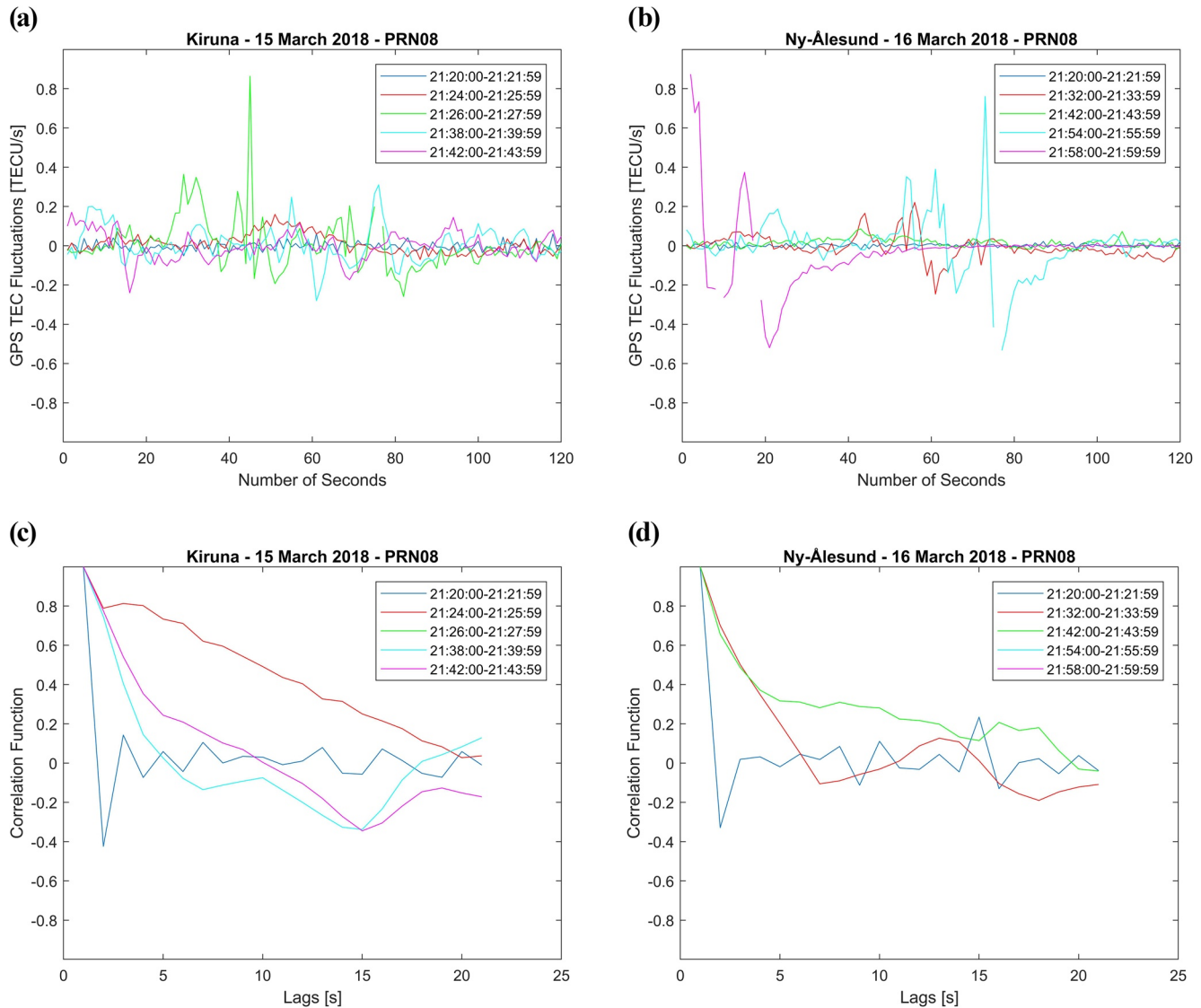
(a)

(b)

(c)

(d)

Figure 11. Details of the autocorrelation function in specific time intervals for PRN08. (a) TEC fluctuations for PRN08 observed from Kiruna, Case Study A March 15, 2018, in various 2-min intervals extracted from Figure 10a. (b) TEC fluctuations for PRN08 observed from Ny-Ålesund, Case Study B March 16, 2018, in various 2-min intervals extracted from Figure 10b. (c) Autocorrelation function, calculated over 2 min, corresponding to the TEC fluctuations illustrated in Figure 11a. (d) Autocorrelation function, calculated over 2 min, corresponding to the TEC fluctuations illustrated in Figure 11b.

irregularities detected on electron density profiles in the auroral (Case Study A) and polar (Case Study B) ionospheres. Structures in the vertical electron density profiles were detected both in the presence of particle precipitation (Figure 5, Case Study A) and of a polar plasma patch (Figure 7, Case Study B): Enhancements in TEC fluctuations were consistent with electron density structures extending over a wider altitude interval in both cases.

In order to investigate this aspect further, the electron density profiles measured by both EISCAT and ESR were therefore integrated along height h between 100 and 400km of altitude to obtain a vertical TEC (TEC$_{rad}$) during each profile or every 1 min (given a calibration interval of 60 s) is given in Equation 7, as follows:

$$\text{TEC}_{rad}(t_k) = \sum_{j=1}^{M-1} \frac{N_e(h_{j+1}, t_k) + N_e(h_j, t_k)}{2}(h_{j+1} - h_j) \quad [\text{TEC}U] \tag{7}$$

where $N_e(h_j, t_k)$ is the electron density at height h_j and at time t_k, whereas M is the number of electron density values between 100 and 400 km of altitude.

Temporal radar TEC fluctuations could be estimated by differentiating the vertically integrated electron density profiles with respect to time as shown in Equation 8:

$$\frac{\text{TEC}_{\text{rad}}}{\Delta t}\left(t_k\right) = \frac{\text{TEC}_{\text{rad}}\left(t_k\right) - \text{TEC}_{\text{rad}}\left(t_{k-1}\right)}{1\,\text{min}}\Big[\text{TEC}U/\text{min}\Big] \qquad (8)$$

The radar TEC fluctuations $\text{TEC}_{\text{rad}}/\Delta t$ are shown in Figure 12a (EISCAT, Case Study A) and Figure 12b (ESR, Case Study B).

The question is to which spatial scales of the irregularities these TEC fluctuations may refer to. Scatter plots of radar TEC fluctuations as a function of the distance between consecutive radars' beams pierce points at 350 km of altitude and 100km of altitude are illustrated in Figures 12c and 12e (EISCAT, Case Study A) and 12 (d and f) (ESR, Case Study B). In these scatter plots, various clusters of points can be noticed: the various clusters are associated with the different beams' positions (at different azimuth and elevation angles) sampling the volume traversed by various GPS ray paths. The cluster at zero distance refers to the times when the beams were maintained in the same position for two consecutive minutes (the distance between consecutive pierce points is not exactly zero due to an inherent relative error of a few percent in the radars' azimuth estimate–the beams were nevertheless profiling along the same direction in these cases). This cluster detects temporal variations in the ionospheric irregularities along a given spatial direction. Given that the range resolution of the beams increases with altitude from a few kilometres in the E region to a few tens of kilometres in the F region (Figure 12g for Case Study A and Figure 12h for Case Study B), the radar TEC fluctuations clustered at zero pierce points distance are associated with electron density structures with larger scale sizes (i.e., between a few kilometres in the E region to a few tens of kilometres in the F region).

Other clusters occur at higher spatial distances because after two consecutive minutes along the same direction the beams were re-positioned along different azimuth/elevation angles (Figures 2 and 3), hence giving a higher distance between consecutive pierce points. These clusters detect spatial and temporal variations in the ionospheric irregularities occurring within the volume sampled: these spatial variations are due to the combination between the size of the irregularities, the temporal variations along a given spatial direction, and the spatial variations due to the change in position of the beams. This type of ambiguity cannot be resolved by EISCAT UHF/ESR measurements: It is expected to be resolved by using EISCAT_3D in the future. Nevertheless, the clusters occurring at higher spatial distances are consistent with enhancements in TEC fluctuations visible on various GPS ray paths from different ground stations surrounding EISCAT UHF/ESR, suggesting that irregularities likely form over large spatial distances and with a patchy spatial distribution (to account for differences between various GPS ray paths).

Therefore, in relation to question (a) the irregularities detected by means of EISCAT during particle precipitation in the auroral ionosphere (Case Study A) and by means of ESR during the transit of a plasma patch in the polar ionosphere (Case Study B) appear to have sizes between a few kilometres in the E region to a few tens of kilometres in the F region and are likely to occur over spatial distances of up to approximately 400 km in the E region and up to approximately 800 km in the F region (as inferred by separation distances in Figures 5 and 7). These irregularities were found to introduce enhancements in GPS TEC fluctuations when extending between the E and F regions. In relation to question (b), enhancements in GPS TEC fluctuations occurred over longer temporal scales, which is consistent with the fact that GPS ray paths traversed larger-scale irregularities in the presence of both particle precipitation and a polar patch.

The two considerations made for both GPS TEC fluctuations and the irregularities detected through EISCAT UHF/ESR and the evidence contained in Figures 10–12 indicate that the effect introduced on GPS TEC fluctuations by inhomogeneous and intermittent particle precipitation in the auroral and polar ionospheres as well as by a plasma patch in the polar ionosphere is very similar. That is, the temporal fluctuations in GPS TEC are enhanced over very similar temporal scales in both cases because of the combination between GPS orbits and the characteristics (i.e., patchy distribution and dynamics) of the irregularities in both the auroral and polar ionospheres. This indicates an intrinsic limitation, for example, in the capability of monitoring and tracking polar plasma patches through ground GPS observations in the presence of particle precipitation.

The nature of larger-scale irregularities inducing enhancements in TEC fluctuations that occur over longer temporal scales as a result of the combination between the size of the irregularities, their patchy distribution
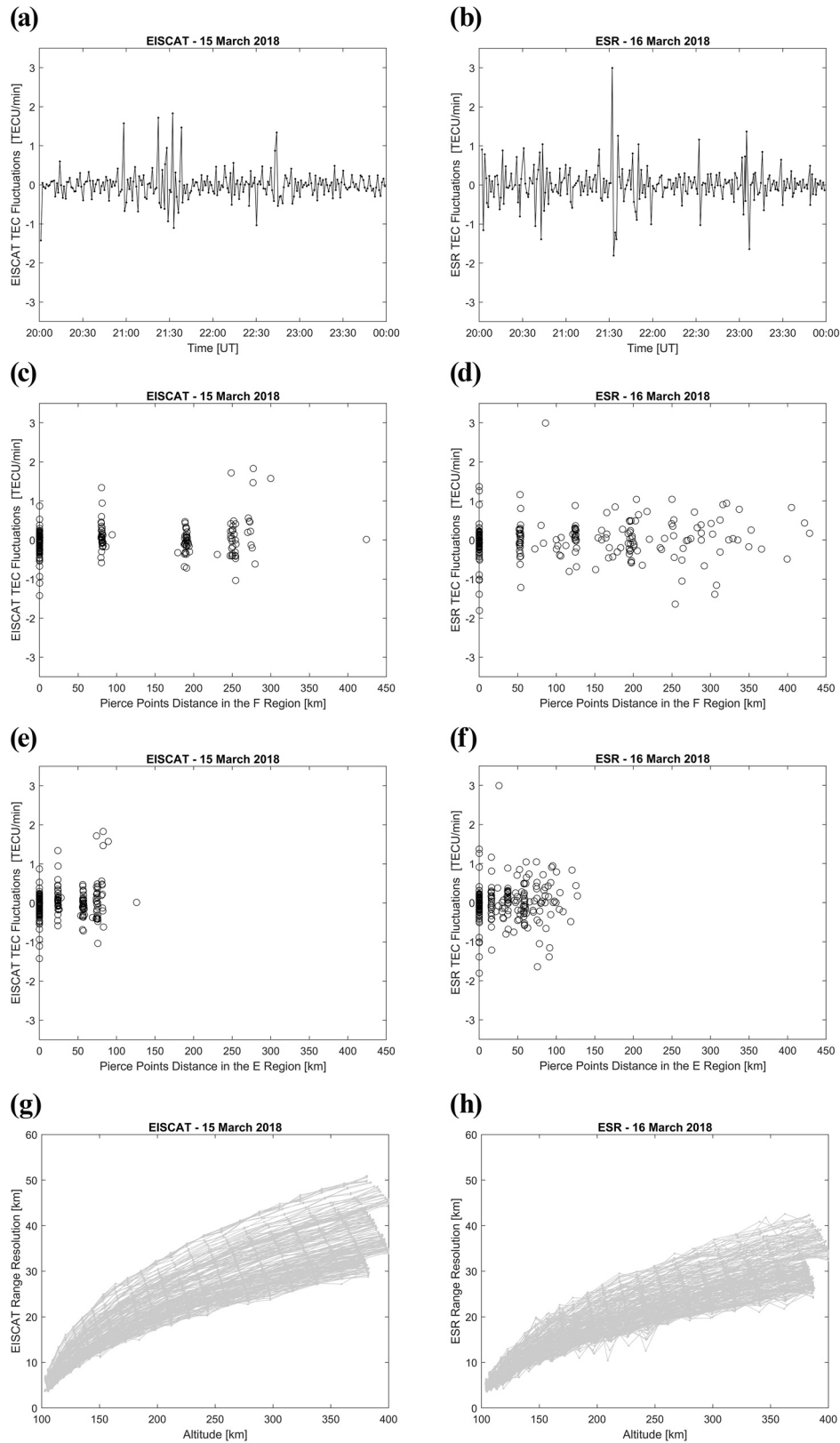
Figure 12.

and dynamics, and the orbits of GPS satellites as described above is consistent with the typical observation of higher phase scintillation indices together with lower intensity scintillation indices in the auroral and polar ionosphere (Forte & Radicella, 2002). This is due to the fact that these slow enhancements in TEC fluctuations correspond to low-frequency increases in the spectral density of the phase fluctuations, hence leading to an overall increase in the phase scintillation index σ_ϕ (Forte & Radicella, 2002).

5. Conclusions

For the first time, the origin of enhancements in temporal TEC fluctuations was found to be in plasma structures occurring in relation to particle precipitation and to a polar plasma patch by using EISCAT UHF/ESR incoherent scatter radars in conjunction with ground GNSS receivers. EISCAT UHF/ESR beams sampled across the volume where various GPS ray paths propagated toward different ground stations in the surrounding.

At auroral and polar latitudes, electron density irregularities capable of inducing enhancements in GPS TEC fluctuations appeared to have sizes between a few kilometres in the E region to a few tens of kilometres in the F region and were observed to occur over spatial distances of up to approximately 400 km in the E region and up to approximately 800 km in the F region. A spatial patchy distribution for these irregularities was consistent with TEC fluctuations observed over various GPS ray paths from different ground stations surrounding EISCAT UHF/ESR.

Enhancements in GPS TEC fluctuations occurred over longer temporal scales, but similar both in the presence of inhomogeneous and intermittent particle precipitation and of a polar plasma patch due to the combination between GPS orbits and the characteristics of the irregularities in both the auroral and polar ionospheres. This aspect introduces a limitation, for example, in the capability of monitoring and tracking polar plasma patches through ground GPS observations in the presence of particle precipitation. Furthermore, the longer temporal scales for enhancements in GPS TEC fluctuations are consistent with the overall observation of higher phase scintillation indices in the auroral and polar ionospheres (Forte & Radicella, 2002).

Data Availability Statement

EISCAT/ESR data are available at http://portal.eiscat.se/schedule/schedule.cgi. The 1-s and 30-s RINEX data were accessed through the International GNSS Service (IGS) from the online archives of the Crustal Dynamics Data Information System (CDDIS), NASA Goddard Space Flight Center, Greenbelt, MD, USA (https://cddis.nasa.gov/Data_and_Derived_Products/GNSS/GNSS_data_and_product_archive.html), http://dx.doi.org/10.5067/GNSS/gnss_daily_o_001. gLAB is a software tool suite develop under a European Space Agency (ESA) Contract by the Research Group of Astronomy and Geomagnetics (gAGE) from the Universitat Politecnica de Catalunya (UPC), is an interactive educational multipurpose package to process and analysis GNSS data (http://www.gage.upc.edu/gLAB). Many thanks to the providers of RTKLIB, which was used to download the 30-s and 1-s RINEX observation and navigation data, used to calculate TEC fluctuations (http://www.rtklib.com/). GPS satellites positions were predicted through the online software utility CalSKY. Source: Arnold Barmettler, www.calsky.com. The authors acknowledge the use of SuperDARN data. SuperDARN is a collection of radars funded by national scientific funding agencies of Australia, Canada, China, France, Japan, South Africa, UK and USA (http://vt.superdarn.org/tiki-index.php).

Figure 12. (a) EISCAT TEC fluctuations as a function of time on March 15, 2018 (Case Study A). (b) ESR TEC fluctuations as a function of time on March 16, 2018 (Case Study B). (c) EISCAT TEC fluctuations as a function of the distance between consecutive pierce points at 350 km of altitude. (d) ESR TEC fluctuations as a function of the distance between consecutive pierce points at 350 km of altitude. (e) EISCAT TEC fluctuations as a function of the distance between consecutive pierce points at 100 km of altitude. (f) ESR TEC fluctuations as a function of the distance between consecutive pierce points at 100 km of altitude. (g) EISCAT range resolution for altitudes between 100 and 400 km and during the entire experiment on March 15, 2018 between 20:00 and 24:00 UT. (h) ESR range resolution for altitudes between 100 and 400km and during the entire experiment on March 16, 2018 between 20:00 and 24:00 UT.

Radio Science

References

Aarons, J. (1982). Global morphology of ionospheric scintillations. *Proceedings of the IEEE*, *70*(4), 360–378. https://doi.org/10.1109/proc.1982.12314

Basu, S., & Basu, S. (1981). Equatorial scintillations—A review. *Journal of Atmospheric and Terrestrial Physics*, *43*(5–6), 473–489. https://doi.org/10.1016/0021-9169(81)90110-0

Beynon, W. J. G., & Williams, P. J. S. (1978). Incoherent scatter of radio waves from the ionosphere. *Reports on Progress in Physics*, *41*(6), 909–955. https://doi.org/10.1088/0034-4885/41/6/003

Chisham, G., & Pinnock, M. (2002). Assessing the contamination of SuperDARN global convection maps by non-F-region backscatter. *Annales Geophysicae*, *20*, 13–28. https://doi.org/10.5194/angeo-20-13-2002

Chisham, G., Yeoman, T. K., & Sofko, G. J. (2008). Mapping ionospheric backscatter measured by the SuperDARN HF radars–Part 1: A new empirical virtual height model. *Annales Geophysicae*, *26*, 823–841. https://doi.org/10.5194/angeo-26-823-2008

Ciraolo, L., Azpilicueta, F., Brunini, C., Meza, A., & Radicella, S. M. (2007). Calibration errors on experimental slant total electron content (TEC) determined with GPS. *Journal of Geodesy*, *81*(2), 111–120. https://doi.org/10.1007/s00190-006-0093-1

Doherty, P., Coster, A. J., & Murtagh, W. (2004). Space weather effects of October–November 2003. *GPS Solutions*, *8*(4), 267–271. https://doi.org/10.1007/s10291-004-0109-3

Forte, B., Coleman, C., Skone, S., Häggström, I., Mitchell, C., Da Dalt, F., et al. (2017). Identification of scintillation signatures on GPS signals originating from plasma structures detected with EISCAT incoherent scatter radar along the same line of sight. *Journal of Geophysical Research: Space Physics*, *122*(1), 916–931. https://doi.org/10.1002/2016ja023271

Forte, B., & Radicella, S. M. (2002). Problems in data treatment for ionospheric scintillation measurements. *Radio Science*, *37*(6), 8-1–8-5. https://doi.org/10.1029/2001rs002508

Forte, B., & Radicella, S. M. (2004). Geometrical control of scintillation indices: What happens for GPS satellites? *Radio Science*, *39*(5), 1–13. https://doi.org/10.1029/2002rs002852

Forte, B., Smith, N. D., Mitchell, C. N., Da Dalt, F., Panicciari, T., Chartier, A. T., & Häggström, I. (2013). Comparison of temporal fluctuations in the total electron content estimates from EISCAT and GPS along the same line of sight. *Annales Geophysicae*, *31*, 745. https://doi.org/10.5194/angeo-31-745-2013

Hernandez-Pajares, M., Juan, J., Sanz, J., Ramos-Bosch, P., Rovira-Garcia, A., Salazar, D., & Hein, G. (2010). The ESA/UPC GNSS-lab tool (glab). *Proc. Of the 5th ESA workshop on satellite navigation technologies (NAVITEC'2010)*. ESTEC, Noordwijk.

Jacobsen, K. S., & Dähnn, M. (2014). Statistics of ionospheric disturbances and their correlation with GNSS positioning errors at high latitudes. *Journal of Space Weather and Space Climate*, *4*, A27. https://doi.org/10.1051/swsc/2014024

Jakowski, N., Wilken, V., Schlueter, S., Stankov, S. M., & Heise, S. (2005). Ionospheric space weather effects monitored by simultaneous ground and space based GNSS signals. *Journal of Atmospheric and Solar-Terrestrial Physics*, *67*(12), 1074–1084. https://doi.org/10.1016/j.jastp.2005.02.023

Jiao, Y., & Morton, Y. T. (2015). Comparison of the effect of high-latitude and equatorial ionospheric scintillation on GPS signals during the maximum of solar cycle 24. *Radio Science*, *50*(9), 886–903. https://doi.org/10.1002/2015rs005719

Jiao, Y., Morton, Y. T., Taylor, S., & Pelgrum, W. (2013). Characterization of high-latitude ionospheric scintillation of GPS signals. *Radio Science*, *48*(6), 698–708. https://doi.org/10.1002/2013rs005259

Keskinen, M. J., & Ossakow, S. L. (1983). Theories of high-latitude ionospheric irregularities: A review. *Radio Science*, *18*(06), 1077–1091. https://doi.org/10.1029/rs018i006p01077

Krypiak-Gregorczyk, A., & Wielgosz, P. (2018). Carrier phase bias estimation of geometry-free linear combination of GNSS signals for ionospheric TEC modeling. *GPS Solutions*, *22*(2), 1–9. https://doi.org/10.1007/s10291-018-0711-4

Lee, J., Morton, Y. J., Lee, J., Moon, H. S., & Seo, J. (2017). Monitoring and mitigation of ionospheric anomalies for GNSS-based safety critical systems: A review of up-to-date signal processing techniques. *IEEE Signal Processing Magazine*, *34*(5), 96–110. https://doi.org/10.1109/msp.2017.2716406

Liu, Y., Li, Z., Fu, L., Wang, J., & Zhang, C. (2020). Studying the ionospheric responses induced by a geomagnetic storm in September 2017 with multiple observations in America. *GPS Solutions*, *24*(1), 3. https://doi.org/10.1007/s10291-019-0916-1

Luo, X., Gu, S., Lou, Y., Xiong, C., Chen, B., & Jin, X. (2018). Assessing the performance of GPS precise point positioning under different geomagnetic storm conditions during solar cycle 24. *Sensors*, *18*(6), 1784. https://doi.org/10.3390/s18061784

Noll, C. E. (2010). The crustal dynamics data information system: A resource to support scientific analysis using space geodesy. *Advances in Space Research*, *45*(12), 1421–1440. https://doi.org/10.1016/j.asr.2010.01.018

Pi, X., Mannucci, A. J., Lindqwister, U. J., & Ho, C. M. (1997). Monitoring of global ionospheric irregularities using the worldwide GPS network. *Geophysical Research Letters*, *24*(18), 2283–2286. https://doi.org/10.1029/97gl02273

Prikryl, P., Jayachandran, P. T., Mushini, S. C., Pokhotelov, D., MacDougall, J. W., Donovan, E., et al. (2010). GPS TEC, scintillation and cycle slips observed at high latitudes during solar minimum. *Annales Geophysicae*, *28*, 1307–1316. https://doi.org/10.5194/angeo-28-1307-2010

Schunk, R., & Nagy, A. (2009). *Ionospheres: Physics, plasma physics, and chemistry*. Cambridge university press.

Spicher, A., Deshpande, K., Jin, Y., Oksavik, K., Zettergren, M. D., Clausen, L. B., & Baddeley, L. (2020). On the production of ionospheric irregularities via Kelvin-Helmholtz instability associated with cusp flow channels. *Journal of Geophysical Research: Space Physics*, *125*(6), e2019JA027734. https://doi.org/10.1029/2019ja027734

Thomas, E. G., & Shepherd, S. G. (2018). Statistical patterns of ionospheric convection derived from mid-latitude, high-latitude, and polar SuperDARN HF radar observations. *Journal of Geophysical Research: Space Physics*, *123*(4), 3196–3216. https://doi.org/10.1002/2018ja025280

Tjulin, A. (2017). *EISCAT experiments*. EISCAT Scientific Association.

Walter, T. (2010). *Effect of ionospheric scintillations on GNSS—A white paper*. SBAS Ionospheric Working Group.

Wernik, A. W., Secan, J. A., & Fremouw, E. J. (2003). Ionospheric irregularities and scintillation. *Advances in Space Research*, *31*(4), 971–981. https://doi.org/10.1016/s0273-1177(02)00795-0

Yeh, K. C., & Liu, C. H. (1982). Radio wave scintillations in the ionosphere. *Proceedings of the IEEE*, *70*(4), 324–360. https://doi.org/10.1109/proc.1982.12313